Large polaron self-trapped states in three-dimensional metal-halide perovskites

Wong, Walter P. D.; Yin, Jun; Chaudary, Bhumika; Chin, Xin Yu; Cortecchia, Daniele; Lo, Shu-Zee A.; Grimsdale, Andrew C.; Mohammed, Omar F.; Lanzani, Guglielmo; Soci, Cesare

2020

Wong, W. P. D., Yin, J., Chaudary, B., Chin, X. Y., Cortecchia, D., Lo, S. A., Grimsdale, A. C., Mohammed, O. F., Lanzani, G. & Soci, C. (2020). Large polaron self-trapped states in three-dimensional metal-halide perovskites. ACS Materials Letters, 2(1), 20-27. https://dx.doi.org/10.1021/acsmaterialslett.9b00276

https://hdl.handle.net/10356/147043

https://doi.org/10.1021/acsmaterialslett.9b00276

Large Polaron Self-trapped States in 3D Metal-Halide Perovskites

Walter P.D. Wong,[1,†] Jun Yin,[2,†] Bhumika Chaudhary,[3,4] Xin Yu Chin,[4] Daniele Cortecchia,[3,4] Shu-Zee A. Lo,[5] Andrew C. Grimsdale,[1] Omar F. Mohammed,[2] Guglielmo Lanzani,[4,6,7] and Cesare Soci[3,4,5*]

[1] *School of Materials Science and Engineering, Nanyang Technological University, 50 Nanyang Avenue, Singapore 639798*

[2] *Division of Physical Science and Engineering, King Abdullah University of Science and Technology, Thuwal 23955-6900, Saudi Arabia*

[3]*Interdisciplinary Graduate School, Nanyang Technological University, 50 Nanyang Avenue, Singapore 639798*

[4] *Energy Research Institute (ERI@N), Research Techno Plaza, X-Frontier Block, Level 5, 50 Nanyang Drive, Singapore 637553*

[5] *Division of Physics and Applied Physics, School of Physical and Mathematical Sciences, Nanyang Technological University, 21 Nanyang Link, Singapore, 637371*

[6] *Dipartimento di Fisica, Politecnico di Milano, Piazza Leonardo da Vinci 32, Milano, Italy*

[7] *CNST@PoliMi, Istituto Italiano di Tecnologia (IIT), Via Giovanni Pascoli 70/3, Milano, Italy*

[†]These authors contributed equally

*Corresponding author: csoci@ntu.edu.sg

Materials and Methods

Sample Preparation

$MAPbI_3$ precursor solutions with concentration 20 wt% and 40 wt% were prepared by dissolving stoichiometric amounts of methylammonium iodide (MAI, Dyesol Inc) and lead iodide (PbI_2, 99.99%, TCI) in anhydrous N,N-dimethylformamide (DMF, Sigma-Aldrich). Calcium Fluoride and intrinsic Silicon substrates were sonicated in acetone and isopropyl alcohol (IPA) for 15 minutes followed by 30 minutes of UV/ozone treatment. The substrates were then transferred into a N_2 filled glovebox with H_2O and O_2 levels <1 ppm. The precursor solution was spin-coated on the substrates at 4000 rpm for 30s; toluene dripping was performed after 4s to obtain smooth, high-quality films. The substrates were subsequently annealed at 100^o C for 15 minutes. 40 wt% solutions were utilised in PIA measurements to improve the signal to noise ratio while 20 wt% solutions were used for transient absorption and fast photocurrent measurements.

Steady-State Photoinduced Absorption

Photoinduced absorption measurements were carried out in a Bruker V80v FTIR spectrometer using a solid-state pump laser (λ=532 nm) with intensity of ~200 mW/cm. 40 wt% sample was utilized for measurement in the MIR and NIR range while 20 wt% sample was utilized for the visible regime. cw-PIA measurements were carried out at low temperature (78 K) using a Helitran cryostat cooled by liquid nitrogen, pumped at a base pressure of $\sim 5.0\times10^{-5}$ mbar. Four different detectors were used to probe the 3 distinct spectral regimes: Deuterated Triglycine Sulfate (DTGS) and Mercury Cadmium Telluride (MCT) to probe the mid-infrared regime, Indium Gallium Arsenide (InGaAs) to probe near-infrared, and Silicon to probe the visible regime. A notch filter at 532 nm was used for measurements in the visible regime to eliminate pump laser scattering, while a 650 nm band pass filter or a double-polished Silicon wafer were

utilized for NIR and MIR measurements, respectively. The FTIR spectrometer operated in rapid scan mode. Transmittance spectra were recorded under photoexcitation, T_{on}, and without photoexcitation, T_{off}. PIA spectra were then derived as $-\Delta T/T = -(T_{off}-T_{on})/T_{off} \approx \Delta\alpha \cdot d$. where $\Delta\alpha$ is the differential absorption coefficient and d is the film thickness. Total 8000 T_{on} and T_{off} scans each were collected and averaged to obtain the desired signal-to-noise ratio.

Transient Absorption

A commercial regenerative amplifier system (Quantronix Integra-C) was used as the laser source at the repetition rate of 1 kHz at 810 nm and pulse width of around 100 fs. A commercial spectrometer, Jobin Yvon CP140-104, equipped with a silicon photodiode array was used to record the transient absorption spectra (Entwicklungsbüro Stresing). A portion of the laser beam was split to generate the 400 nm pump beam using a 1 mm thick BBO crystal cut at 29.2°. White probe light was generated using a sapphire crystal coupled with a 750 nm short pass filter just sufficient to attenuate 800 nm generation beam without saturating the camera and thus, the output spectrum was sensitive from 550 to 830 nm. Another long pass filter with cut-off wavelength of 450 nm was used after the sample to avoid saturation of the camera by the intense pump beam.

Global fitting of the resulting spectral decays was performed using the R-package TIMP on Glotaran interface,[58] with multiple sequential exponential decays. Dispersion compensation was conducted by fitting 2nd order dispersion relationship central at 755 nm in conjunction with the interested multiple exponential decay function. Convergence of the numerical fitting is ensured by multiple rounds of numerical fitting using calculated parameters from previous round, until all parameters stabilize. Overall goodness of the fitting is indicated by the final residual error of 0.489 after stabilization, with no temporal and spectral trend in residue plots.

Steady-State Photocurrent

Measurements were performed using conventional amplitude modulation technique in a setup equipped with a Xe lamp source, a monochromator (Horiba iHR550) which disperses light in the wavelength range of 300-900 nm, a mechanical chopper (Stanford SR570), a voltage source (Keithley 6487), and a lock-in amplifier (Stanford SR830). The chopper modulation frequency was 138 Hz, and the lock-in time constant was 300 ms, corresponding to 0.42 Hz equivalent noise bandwidth. Before the measurement, the monochromatic light power/intensity was obtained using a reference calibrated Si photodiode. The responsivity (R_i) so obtained is the product of incident power on the sample surface (P_i) and measured photocurrent (iP_h).

Trap-limited (long-time) charge carrier mobility was estimated using the classical Drude model, according to which the steady-state photocurrent is given by $J_{PC}(t) = e\mu\Delta n(t)F$, where e is the elementary charge, μ is the charge carrier mobility, Δn is the photogenerated carrier density, and F is the applied electric field. The optical generation rate of free carriers can be written as $g(z) = -\eta \frac{1}{\hbar\omega}\frac{dI}{dz} = \eta(1-R)\frac{1}{\hbar\omega}\alpha I_0 e^{-\alpha z}$, where α is the material's absorption coefficient, R its reflectance, I_0 the incident illumination intensity, η the charge carrier photogeneration quantum efficiency, and $\hbar\omega$ the excitation photon energy. Under steady-state condition, $\Delta n(t) = g\tau = constant$, where τ is the characteristic carrier lifetime. Thus, assuming unitary quantum efficiency and complete photon absorption, $J_{PC}(t) = e\mu\tau F\int_0^d g(z)\,dz = \frac{I_0 e}{\hbar\omega}F\mu\tau$. As such, with illumination intensity of I_0 = 18.5 μW/cm^2 at photon energy of 1.68 eV, the corresponding mobility-lifetime product is of the order of $\mu\tau = 1.96\times10^{-3}\ cm^2V^{-1}$; assuming a carrier lifetime of $\tau \approx 1-10\ ms$ (limited by the cw-PIA modulation frequency), we estimate $\mu_{ss} = 0.2-2\ cm^2V^{-1}s^{-1}$.

Transient Photocurrent

The setup utilizes the same femtosecond pump laser as for transient absorption measurements, frequency doubled to the excitation wavelength of 400 nm. Gold contacts were deposited via a shadow mask to form a 50 Ω Auston photoconductive switch, with gap of 0.1 mm and width of 0.6 mm. Measurements were performed in a vacuum chamber focusing 5 mW laser beam power on a 1.5 x 10^{-3} cm^2 spot size. An external bias of 20 V was supplied by a picoammeter/voltage source (Keithley 6487). The transient photocurrent signal was recorded using a real-time high-speed oscilloscope (Teledyne Lecroy LabMaster 10 Zi-A) equipped with a 65 GHz sampling channel, connected after a Mini-Circuit DC-AC splitter to prevent DC current leakage.

The early-time mobility was estimated from the peak transient photocurrent, $I_{peak} = \eta\phi\mu(1-R)\frac{E_p e}{\hbar\omega}\frac{V}{d^2}$, where η is the photogeneration quantum efficiency, ϕ is the probability to escape fast recombination, μ is the charge carrier mobility, E_p is the energy of the laser pulse, V is applied voltage, d is the distance between the electrodes and $\hbar\omega/e$ the photon energy in Volts. We assumed unitary charge generation quantum yield and estimated the probability to escape fast recombination to be 0.1 since the excitation density is on the order of 10^{18} cm^{-3}.[1] We estimated reflectance from Fresnel equation, $R = \left|\frac{1-\eta}{1+\eta}\right|^2$ using $\eta = 2.3$,[2] hence $1 - R = 0.84$. Using experimental values for the excitation fluence of 0.64 mJ cm^{-2} and d=100 μm, we finally derived $\mu \approx 6$ $cm^2V^{-1}s^{-1}$.

Computational Methods

The density functional theory (DFT) calculations were carried out at generalized gradient approximation (GGA)/Perdew-Burke-Ernzerhof (PBE) level using the projector-augmented wave (PAW) method as implemented in the Vienna Ab initio Simulation (VASP) package.[3-4] The plane-wave basis set cutoff of the wavefunctions was set at 400 eV and a uniform grid of

6×6×6 *k*-mesh in the Brillouin zone was employed to optimize the crystal structure of $MAPbI_3$. The van der Waals functional vdW-DF was also included for the structural optimizations and electronic property calculations. The resulting crystal parameter of tetragonal-phase $MAPbI_3$ is a = 8.68 Å, b = 8.67 Å, c = 12.8 Å. A 3×3×3 supercell containing 1296 atoms was used for the large polaron calculations, and the Brillouin zone was sampled by the Γ point. The atomic positions of $MAPbI_3$ supercells in neutral and charged states were fully relaxed until the supercells with forces on each atom less than 0.01 eV/Å. The charge density distribution of valence band maximum (VBM)/conduction band minimum (CBM) for $MAPbI_3$ supercells were used to describe the positive/negative polaron feature. The effective masses for electron (m_e^*) and hole (m_h^*) were estimated by fitting of the dispersion relation of $m^* = \hbar^2 \left[\frac{\partial^2 \varepsilon(k)}{\partial k^2}\right]^{-1}$ from band structures (Figures S1a and S1b) along the directions Γ-X, Γ-Z and Γ-M for tetragonal phase and Γ-X and Γ-Z for orthorhombic phase. The optical dielectric function was calculated using *random phase approximation* (RPA) method as implemented in VASP (Figures S1c and S1d).

The infrared and Raman vibrational mode positons and intensities, at the Γ point of the first Brillouin zone, were calculated on orthorhombic-phase $MAPbI_3$ using the *Phonon* code as implemented in the *Quantum Espresso* package.[5] The local density approximation (LDA) exchange-correlation functional with norm-conserving pseudopotentials was used based on the optimized natural and charged structures. The plane-wave expansion cutoff for the wavefunctions was set at 100 Ry. Uniform grids of 12×12×8 Monkhorst-Pack scheme were used for the k-point sampling together with self-consistency threshold of 10^{-14} Ry.

Polaron Mobility

The electron-phonon coupling is described by the dimensionless Fröhlich parameter α, defined as:

$$\alpha = \frac{1}{4\pi\varepsilon_0}\frac{e^2}{\hbar}\left(\frac{1}{\varepsilon_\infty}-\frac{1}{\varepsilon_s}\right)\sqrt{\frac{m}{2\hbar\omega}}$$

where ε_0 is the dielectric constant of vacuum; ε_∞ and ε_s are optical and static dielectric constants, respectively; e is the charge of carrier; $2\pi\hbar$ is Planck's constant; m is the bare electron band effective mass; and ω is the characteristic angular frequency of the longitudinal optical (LO) phonon mode, which is calculated from the Im[$1/\varepsilon(\omega)$] spectra in far-infrared region, as presented in Figure S2.

Ōsaka provided the finite-temperature free energies of the coupling electron-phonon system by extending Feynman's athermal variational solution. The self-free energy of polaron, F, under the phono occupation factor $\beta = \omega/k_B T$ was calculated with two parameters v (a unit of ω, the frequency of relation motion between a charge and a coupled LO phonon) and w (a unit of ω).[6-7] The v and w were numerically solved by giving the minimum $F = -(A + B + C)$, where[8]

$$A = \frac{3}{\beta}\left[ln\left(\frac{v}{w}\right)-\frac{ln(2\pi\beta)}{2}-ln\frac{sinh\left(\frac{v\beta}{2}\right)}{sinh\left(\frac{w\beta}{2}\right)}\right];$$

$$B = \frac{\alpha v}{\sqrt{\pi[exp(\beta)-1]}}\int_0^{\frac{\beta}{2}}\frac{exp(\beta-x)+exp(x)}{\sqrt{w^2x\left(1-\frac{x}{\beta}\right)+\frac{Y(x)(v^2-w^2)}{v}}}dx;$$

$$Y(x) = \frac{1}{1-exp(-v\beta)}[1+exp(-v\beta)-exp(-vx)-exp\{v(x-\beta)\}];$$

$$C = \frac{3\left(v^2-w^2\right)}{4v}\left(coth\left(\frac{v\beta}{2}\right)-\frac{2}{v\beta}\right);$$

Then the Polaron mobility can be described as:[9-10]

$$\mu = \frac{3\sqrt{\pi}e}{2\pi\omega m\alpha_{e-ph}}\frac{sinh(\beta/2)}{\beta^{5/2}}\frac{w^3}{v^3}\frac{1}{K};$$

$$\text{where } K = \int_0^\infty \frac{cos(u)}{\left(u^2+a^2-bcos(vu)\right)^{3/2}} du;$$

$$a^2 = \left(\frac{\beta}{2}\right)^2 + \left(\frac{v^2-w^2}{w^2 v}\right)\beta coth\left(\frac{\beta v}{2}\right);$$

$$b = \left(\frac{v^2-w^2}{w^2 v}\right)\frac{\beta}{sinh\left(\frac{\beta v}{2}\right)};$$

Free Carrier Mobility

The free carrier mobilty was calculated by the semi-classical Boltzmann transport theory.[10] Only the contribution of acoustic phonons was considered in evaluating scattering lifetime, where the charge carrier density (n) and mobility (μ) are approximated as[11-12]

$$n = \frac{(2m^* k_B T)^{3/2}}{2\pi^2\hbar^3}\ {}^0F_0^{3/2};\ \mu = \frac{2\pi\hbar^4 eB}{m_I^*\left(2m_b^* k_B T\right)^{3/2}\Xi^2}\frac{3\,{}^0F_{-2}^1}{{}^0F_0^{3/2}};$$

$$\text{where } {}^nF_l^m = \int_0^\infty \left(-\frac{\partial f}{\partial \zeta}\right)\zeta^n(\zeta+\alpha\zeta^2)^m[(1+2\alpha\zeta)^2+2]^{l/2}d\zeta;$$

$$f = 1/\left(e^{\zeta-\xi}+1\right);\ \alpha = k_B T/E_g,$$

k_B is the Boltzmann constant, e is the elementary charge, T is the temperature, $2\pi\hbar$ is the Planck constant, and ξ is the reduced chemical potential; m^* is the density of state effective mass, m_I^* is the conductivity effective mass, m_b^* is the band effective mass; B is the bulk modulus ($B = \partial^2 E/\partial V^2$), $\Xi_{e-p/h-p}$is the electron-phonon (or hole-phonon) coupling energy ($\Xi_{e-p/h-p} = V_0\left(\Delta E_{CBM/VBM}/\Delta V\right)$, n, m, and l power integer indices, E_g is the electronic band gap, and ζ is the reduced carrier energy.

Table S1. The parameters for calculating polaron mobility. Optical and static dielectric constants (ε_∞ and ε_S), angular frequencies of a characteristic LO phonon mode (ω), average hole/electron effective masses of bare electron bands (m^*), electron-phonon coupling constant (α), phono occupation factor (β), positive/negtive polaron mass ($m^*_{polaron}$) and positive/negative polaron mobility ($\mu_{polaron}$) for tetragonal- and orthorhombic-phase $MAPbI_3$.

Compound	Type	ε_∞	ε_S	$\omega/2\pi$ (THz)	m^* ($\times m_0$)	α	β	$m^*_{polaron}$ ($\times m_0$)	$\mu_{polaron}$ ($cm^2/V\cdot s$)
$MAPbI_3$ (300K, Tetragonal)	Positive	4.73	27.31	4.11	0.210	2.356	0.661	0.507	215.38
	Negative				0.200	2.299		0.492	225.93
$MAPbI_3$ (78K, Orthorhombic)	Positive	4.53	23.59	4.86	0.210	2.208	1.396	0.468	497.93
	Negative				0.187	2.084		0.435	550.68

Table S2. The parameters for calculating free carrier mobility. Band (m_b^*), conductivity (m_l^*) and density of state (m^*) effective mass, hole/electron-phonon coupling (Ξ), and bulk modulus (B), and free hole/electron mobility ($\mu_{carrier}$) for tetragonal- and orthorhombic-phase $MAPbI_3$.

Compound	Type	m_b^*	m_l^*	m^*	Ξ	B	$\mu_{carrier}$ ($cm^2/V\cdot s$)
$MAPbI_3$ (300K, Tetragonal)	Positive	0.198	0.196	0.210	10.268	3.303	332.2
	Negative	0.185	0.184	0.200	7.975		630.5
$MAPbI_3$ (78K, Orthorhombic)	Positive	0.220	0.215	0.210	10.869	3.427	1491.6
	Negative	0.171	0.166	0.187	8.051		5122.0

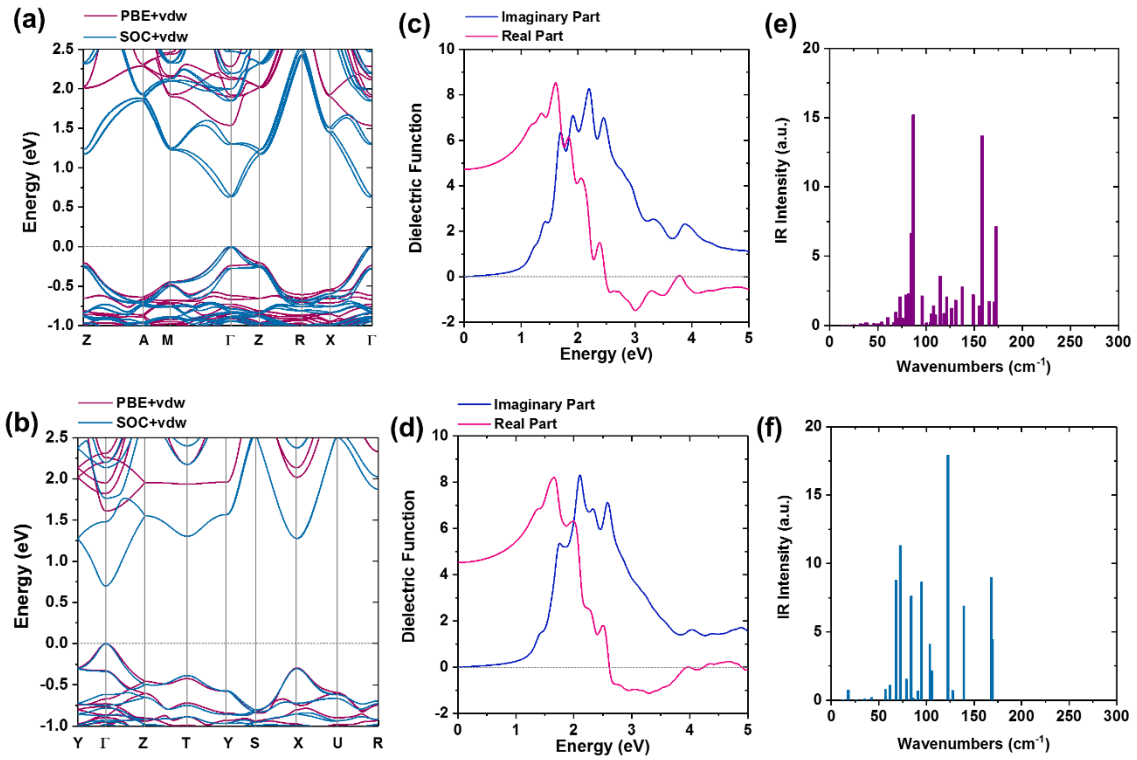

Figure S1. Electronic and optical properties of $MAPbI_3$. (a, b) calculated electronic band structures, (c, d) real part (in red) and imaginary part (in blue) of dielectric function, and (e, f) far-infrared vibrational modes and intensity for tetragonal-phase (up) and orthorhombic-phase (down) $MAPbI_3$.

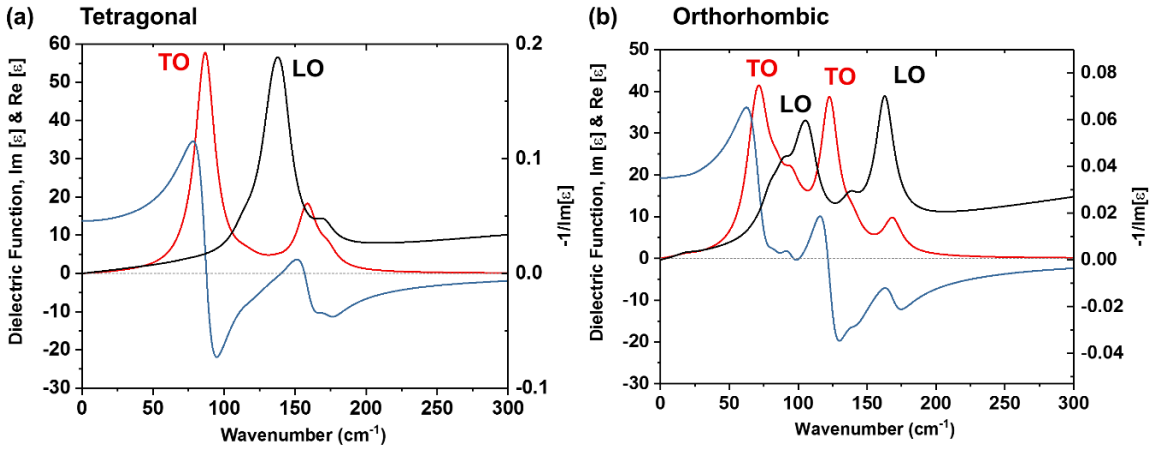

Figure S2. Far-infrared optical response of $MAPbI_3$. Calculated real part (in red), imaginary part (in blue) of dielectric function, and imaginary part of the inverse dielectric function (in black) for (a) tetragonal-phase and (b) orthorhombic-phase $MAPbI_3$.

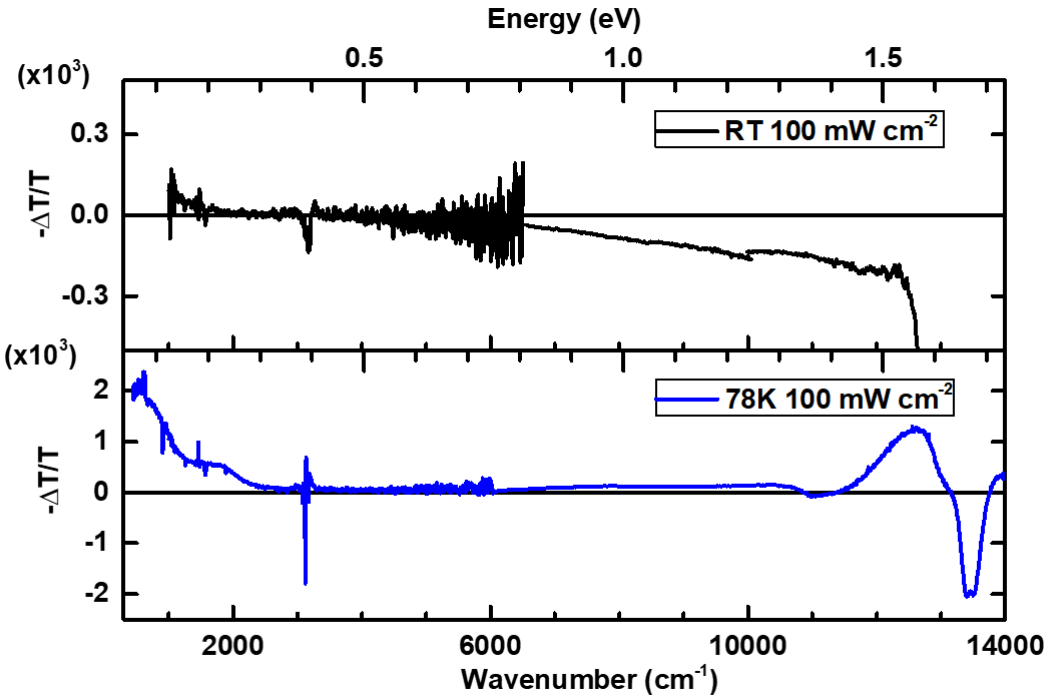

Figure S3. Comparison of photoinduced absorption spectrum at room temperature (298 K, top panel) and low temperature (78 K, bottom panel) with 523nm laser (green laser) excitation of 100 mWcm^{-2}. Note firstly, the difference in the magnitude of photoinduced absorption peaks between the two spectrums and secondly the disappearance of the MIR peaks.

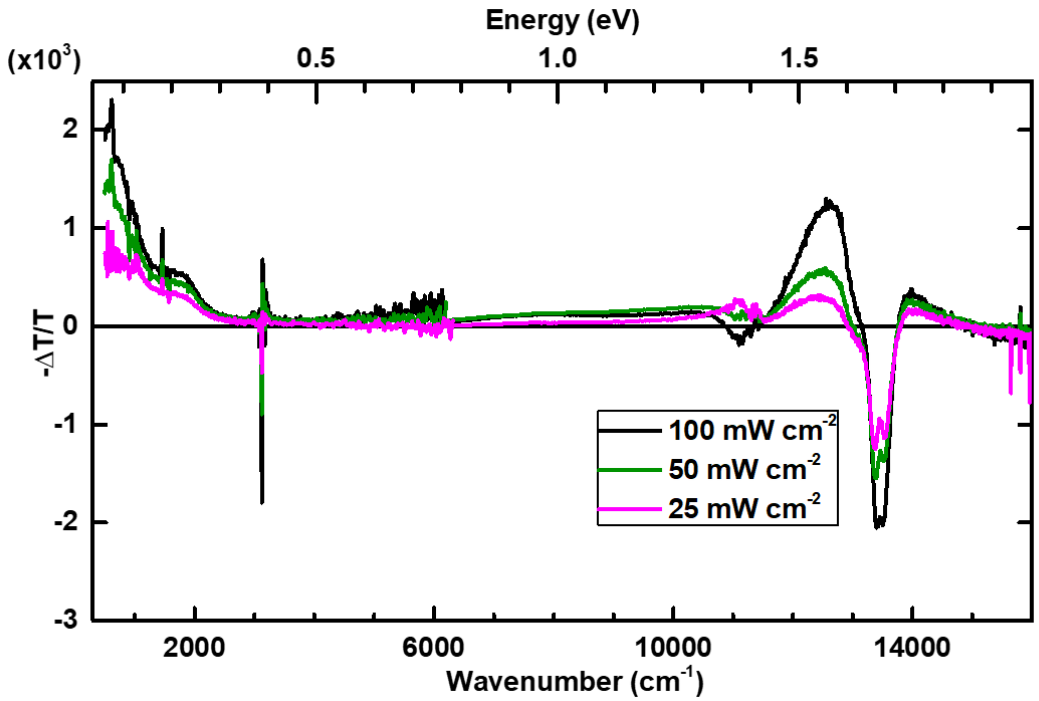

Figure S4. Comparison of photoinduced absorption spectrum at 78 K with different excitation intensities. It can be observed clearly that with a decreasing excitation intensity, the photoinduced absorption (and bleaching) peaks also decreases while maintaining the key MIR features.

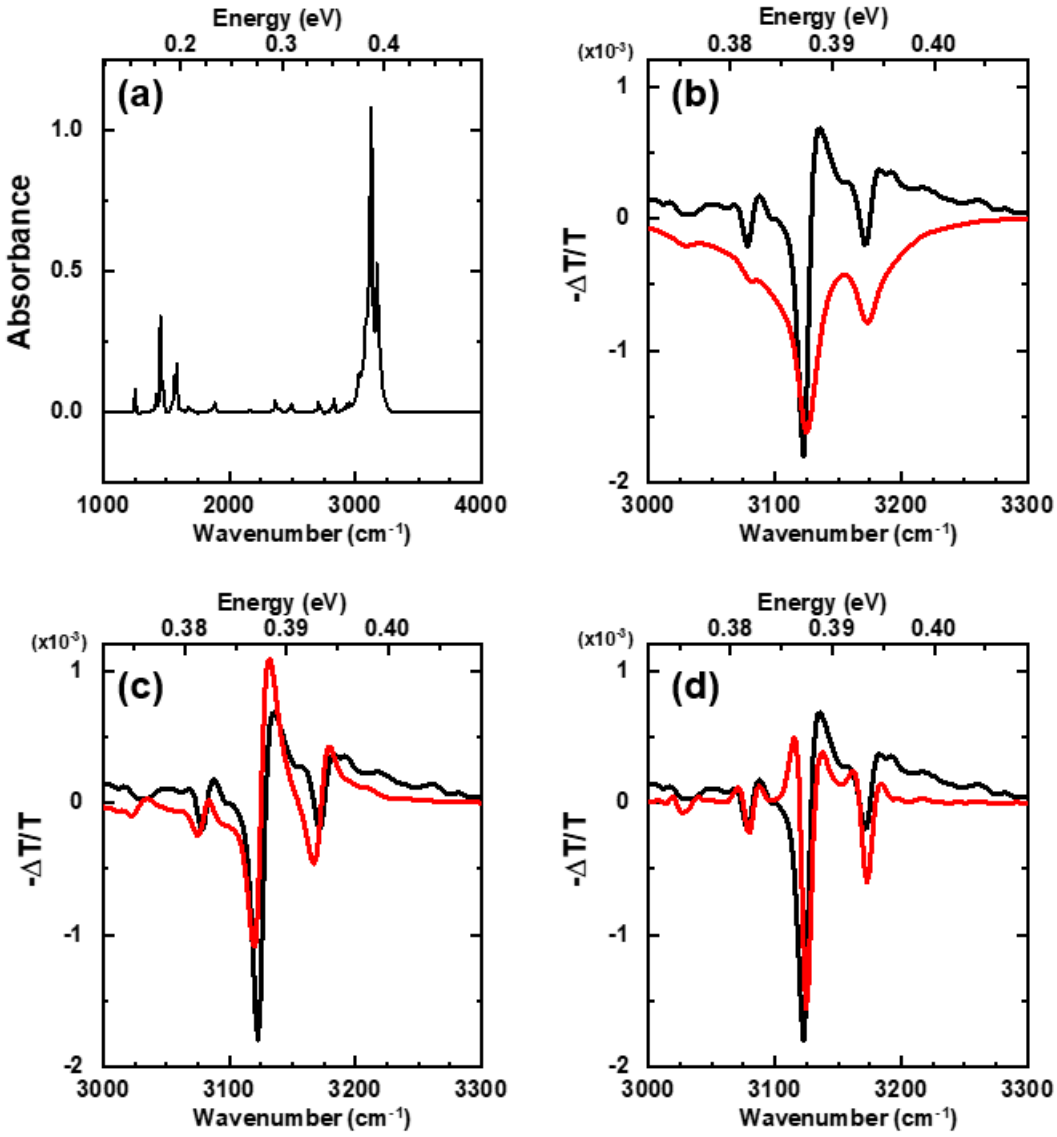

Figure S5. (a) Steady-state MIR spectra of $MAPbI_3$ at 78 K. The experimental curve (black line) is fitted to (red lines): (b) the 0th order derivative: $f_{der}(\bar{\nu}) = -0.0015 f(\bar{\nu})$, (c) the 1st order derivative: $f_{der}(\bar{\nu}) = -0.02\, f'(\bar{\nu})$, and (d) the 2nd order derivative: $f_{der}(\bar{\nu}) = 0.11\, f''(\bar{\nu})$.

References

1. D'Innocenzo, V.; Grancini, G.; Alcocer, M. J. P.; Kandada, A. R. S.; Stranks, S. D.; Lee, M. M.; Lanzani, G.; Snaith, H. J.; Petrozza, A., Excitons versus Free Charges in Organo-Lead Tri-halide Perovskites. *Nat. Commun.* **2014**, *5*, 3586.
2. Löper, P.; Stuckelberger, M.; Niesen, B.; Werner, J.; Filipič, M.; Moon, S.-J.; Yum, J.-H.; Topič, M.; De Wolf, S.; Ballif, C., Complex Refractive Index Spectra of $CH_3NH_3PbI_3$ Perovskite Thin Films Determined by Spectroscopic Ellipsometry and Spectrophotometry. *J. Phys. Chem. Lett.* **2015**, *6* (1), 66-71.
3. Kresse, G.; Furthmuller, J., Efficiency of Ab-initio Total Energy Calculations for Metals and Semiconductors using a Plane-wave Basis Set. *Comput. Mater. Sci.* **1996**, *6* (1), 15-50.
4. Kresse, G.; Joubert, D., From Ultrasoft Pseudopotentials to the Projector Augmented-wave Method. *Phys. Rev. B* **1999**, *59* (3), 1758-1775.
5. Giannozzi, P.; Baroni, S.; Bonini, N.; Calandra, M.; Car, R.; Cavazzoni, C.; Ceresoli, D.; Chiarotti, G. L.; Cococcioni, M.; Dabo, I.; Dal Corso, A.; de Gironcoli, S.; Fabris, S.; Fratesi, G.; Gebauer, R.; Gerstmann, U.; Gougoussis, C.; Kokalj, A.; Lazzeri, M.; Martin-Samos, L.; Marzari, N.; Mauri, F.; Mazzarello, R.; Paolini, S.; Pasquarello, A.; Paulatto, L.; Sbraccia, C.; Scandolo, S.; Sclauzero, G.; Seitsonen, A. P.; Smogunov, A.; Umari, P.; Wentzcovitch, R. M., QUANTUM ESPRESSO: a modular and open-source software project for quantum simulations of materials. *J. Phys.: Condens. Matter* **2009**, *21* (39), 395502.
6. Feynman, R. P., Slow Electrons in a Polar Crystal. *Phys. Rev.* **1955**, *97* (3), 660-665.
7. Osaka, Y., Polaron State at a Finite Temperature. *Prog. Theor. Phys.* **1959**, *22* (3), 437-446.
8. Miyata, K.; Meggiolaro, D.; Trinh, M. T.; Joshi, P. P.; Mosconi, E.; Jones, S. C.; De Angelis, F.; Zhu, X. Y., Large Polarons in Lead Halide Perovskites. *Sci Adv* **2017**, *3* (8), e1701217.
9. Frost, J. M., Calculating Polaron Mobility in Halide Perovskites. *Phys. Rev. B* **2017**, *96* (19).
10. Wang, H.; Pei, Y. Z.; LaLonde, A. D.; Snyder, G. J., Weak Electron-Phonon Coupling Contributing to High Thermoelectric Performance in n-type PbSe. *Proc. Natl. Acad. Sci.* **2012**, *109* (25), 9705-9709.

11. He, Y. P.; Galli, G., Perovskites for Solar Thermoelectric Applications: A First Principle Study of $CH_3NH_3Al_3$ (A = Pb and Sn). *Chem. Mater.* **2014**, *26* (18), 5394-5400.
12. Chin, X. Y.; Cortecchia, D.; Yin, J.; Bruno, A.; Soci, C., Lead Iodide Perovskite Light-emitting Field-effect Transistor. *Nat. Commun.* **2015**, *6*, 7383.